

Dendritic Computing with Multi-Gate Ferroelectric Field-Effect Transistors

A N M Nafiul Islam,¹ Xuezhong Niu,² Jiahui Duan,² Shubham Kumar,² Kai Ni,² and Abhronil Sengupta,^{1*}

¹ School of Electrical Engineering & Computer Science, The Pennsylvania State University, University Park, PA 16802, USA

² Department of Electrical Engineering, University of Notre Dame, Notre Dame, IN 46556, USA

*E-mail address: sengupta@psu.edu

Abstract

Although inspired by neuronal systems in the brain, artificial neural networks generally employ point-neurons, which offer far less computational complexity than their biological counterparts. Neurons have dendritic arbors that connect to different sets of synapses and offer local non-linear accumulation – playing a pivotal role in processing and learning. Inspired by this, we propose a novel neuron design based on a multi-gate ferroelectric field-effect transistor that mimics dendrites. It leverages ferroelectric nonlinearity for local computations within dendritic branches, while utilizing the transistor action to generate the final neuronal output. The branched architecture paves the way for utilizing smaller crossbar arrays in hardware integration, leading to greater efficiency. Using an experimentally calibrated device-circuit-algorithm co-simulation framework, we demonstrate that networks incorporating our dendritic neurons achieve superior performance in comparison to much larger networks without dendrites ($\sim 17\times$ fewer trainable weight parameters). These findings suggest that dendritic hardware can significantly improve computational efficiency, and learning capacity of neuromorphic systems optimized for edge applications.

Introduction

Artificial Intelligence (AI) has become ubiquitous and has revolutionized countless fields. The artificial neural networks (ANNs) at the heart of deep learning algorithms that power these AI systems generally employ a simplified neuron model known as the point neuron (*1*), where a linear summation of all synaptic outputs is performed, followed by a single lumped nonlinear activation function, such as a rectified linear unit, ReLU. This abstraction of the neuron ignoring spatial or structural nuances is vastly different to that seen in nature. In fact, biological neurons exhibit far more complicated functionalities beyond this basic somatic behavior.

A key feature of real neurons is the presence of dendrites — branch-like structures that receive and locally process synaptic inputs before contributing to the neuron’s overall output (Fig. 1(a)). These dendrites are not merely passive conduits; rather, they actively shape input signals through nonlinear, location-specific interactions (*2–4*). Numerous studies have shown that the local plasticity offered by dendrites greatly improves the information processing ability of biological networks and may underlie the brain's superior learning ability (*5–7*). Recent computational efforts in ANNs have shown that these benefits in the biological realm do indeed translate to quantifiable improvements in learning accuracy, generalization, and adaptability across real-world tasks (*8–14*).

Parallel to algorithmic developments, efforts in developing neuromorphic computing hardware have tried to create devices that can mimic the behavior of the brain primitives. Like ANNs, however, they also primarily focus on synaptic and somatic neuronal devices – largely overlooking dendrites. Some prior works have attempted to model dendrites using discrete devices (*15–19*), circuit-level demonstrations (*20, 21*), or simplified architectural modifications (*8, 22*). While these approaches have provided useful insights, they often remain constrained to shallow networks or are limited to processing temporal patterns. They offer no obvious path forward for scaling to deeper neural networks that pioneer the current AI advancements. Furthermore, these methods generally require the inclusion of significant additional peripheral circuitry – sacrificing energy and area efficiency. Thus, the hardware advantages of incorporating dendrites into neural network hardware remain unclear.

In this work, we attempt to answer these questions and propose a singular device that can be employed as a neuron with integrated dendritic branches, operating in the analog regime. Our device is designed to be seamlessly incorporated in crossbar array architectures, which are widely used in neuromorphic systems for their parallelism and density – accelerating efficient computation in deep neural networks. The proposed neuron is based on a multi-gate Ferroelectric Field Effect Transistor (FeFET), shown in Fig. 1(b). The 1T-*n*C device structure consists of a metal-ferroelectric-metal-insulator-semiconductor (MFMIS) stack. The input gates, which represent the dendrite branches, have a thin film Hafnium Zirconium Oxide (HZO) ferroelectric layer with a floating metal gate underneath, shared by all the gates. Below the shared electrode is the thin dielectric oxide layer (HfO₂) followed by the transistor channel, with its source and drain.

The device architecture enables distinct functionalities at different regions. As shown in Fig. 1(c), the non-linear switching characteristic of the ferroelectric layer is utilized as the dendritic non-linearity, while the field effect switching of the channel underneath performs the somatic operation. When a drain voltage is applied, the drain current works as the output of the entire neuron. Channel conductivity is determined by the floating gate potential,

which is dependent on the ferroelectric capacitors. The partial polarization switching of the domains in the ferroelectric material under various amplitudes of programming pulses leads to controlled non-linear charge accumulation on the floating gate, which then exerts its influence in the underlying channel and its conduction characteristics. This mechanism yields a fundamentally different functionality compared to the NAND structure or any previously discussed multi-gate FeFET (19, 23, 24). However, like 3D NAND, the structure can leverage the excellent scalability (25) and back-end-of-line (BEOL) compatibility (26) of the ferroelectric layers to enable 3D integrated architectures (Fig. 1(d)). Coupled with FeFET based synapses (27, 28), the multi-gate FeFET can realize an efficient, adaptive and scalable monolithic neuromorphic platform.

Building on this device innovation, we leverage the intrinsic nonlinearity to design a dendritic deep neural network. We experimentally calibrate a device model with 3-gates and extend it for n -gates and use it to develop a device-circuit-algorithm co-simulation framework to assess the end-to-end impact of the dendritic computation on learning tasks. Our results clearly delineate the advantages afforded by the proposed device – both from a performance and hardware-efficiency perspective and paves a scalable path for next-generation neuromorphic systems that bring AI closer to the brain’s computing paradigm.

Results

Multi-gate FeFET Operation:

We start by analyzing the functionality of the proposed device. Fig. 1(e) shows different gate voltages being applied across the different gate terminals of the device. We denote the terminal voltage, the voltage and charge across the ferroelectric layer of the i -th gate as V_i , $V_{FE,i}$ and Q_i respectively. ϕ_F and Q_F are the floating gate voltage and charge respectively. Q_{MOS} is the charge across the shared floating gate and the channel. Assuming no charge injection occurring during device operation (29), we can write the following equation by equating the charges:

$$Q_F = Q_{MOS} + \sum_{i=1}^N -Q_i \quad (1)$$

Here, N is the total number of gates. The charge across the ferroelectric layer is a summation of the polarization, P_i and the product of the ferroelectric capacitance, C_i and $V_{FE,i}$. Similarly, Q_{MOS} can be written as a product of the floating gate voltage and the oxide capacitance, C_0 . Assuming the initial charge at the floating gate to be zero (i.e., $Q_F = 0$), we can now rewrite (1) as follows:

$$\begin{aligned} C_0 \cdot \phi_F &= \sum_{i=1}^N (P_i + C_i \cdot V_{FE,i}) \\ &= \sum_{i=1}^N (P_i + C_i \cdot (V_i - \phi_F)) \\ &= \sum_{i=1}^N (P_i + C_i \cdot V_i) - \phi_F \cdot \sum_{i=1}^N C_i \end{aligned} \quad (2)$$

Solving for ϕ_F , we get,

$$\phi_F = \frac{\sum_{i=1}^N C_i \cdot V_i}{\sum_{i=0}^N C_i} + \frac{\sum_{i=1}^N P_i}{\sum_{i=0}^N C_i} \quad (3)$$

Here, ϕ_F consists of two terms: one depending on the capacitances while the other depends on the polarization of the ferroelectric layer. It is this latter term that is responsible for the non-linearity of dendrites. The polarization of the i -th gate can be calculated by assuming that the ferroelectric layer consists of multiple independent domains, N_{dom} and employing a Monte Carlo algorithm based ferroelectric model (28, 30).

Each domain in the ferroelectric layer can be polarized in either one of the two stable orientations, generally denoted by $(-1,1)$. Under a time-varying applied electric field, $E_{FE}(t)$, the switching probability, p_k , of the k -th domain with a certain time step, Δt , can be expressed by (31),

$$p_k(t_s < t + \Delta t \mid t_s > t) = 1 - \exp(h_k(t)^\beta - h_k(t + \Delta t)^\beta) \quad (4)$$

Here, t_s is the switching time of the k -th domain considering the domain has not switched before t ; β is the shape parameter of the probability distribution of the activation fields, $E_{a,k}$; h_k is the history parameter that tracks the change of the switching time constant, τ_k , given by (31):

$$h_k(t) = \int_{t_0}^t \frac{dt'}{\tau_k(E_{FE}(t'), E_{a,k})} \quad (5)$$

$$\tau_k(E_{FE}, E_{a,k}) = \tau_0 \exp \left[\left(\frac{E_{a,k}}{E_{FE}} \right)^\alpha \right] \quad (6)$$

The total polarization of each gate's ferroelectric layer, $P_{total,i}$, can be measured by summing up the states of all of the domains at any time, t by:

$$P_{total,i}(t) = \frac{P_S}{M_i} \sum_{k=1}^{M_i} s_k(t) \quad (7)$$

Here, M_i is the total number of domains in the i -th gate's ferroelectric layer; P_S is the saturated polarization of the ferroelectric and s_k denotes the state of the domain (i.e., -1 or $+1$). By combining the ferroelectric polarization model with the transistor charge-voltage equations (Eq. (1-3)) and then finally calculating the resultant drain current, we can self-consistently solve the model to obtain the final output characteristics of our neuron with dendrites.

Experimental Validation and Understanding Impact of Ferroelectric Switching:

To validate and calibrate the discussed model, we fabricated and characterized a 3-gate FeFET device, as shown in Fig. 2(a). Details regarding device fabrication and the measurement setup can be found in the Methods section. We begin by validating the ferroelectric switching behavior of our ferroelectric capacitors (Supplementary Fig. S1—S3) and the FET switching behavior (Supplementary Fig. S4). Next, we measure the device's response to programming voltages of varying amplitudes applied to each gate (Fig. 2(b)). Initially a reset pulse of $-3V$ for $1ms$ is applied to each of the gates to reset all the domains of the ferroelectric layer to the negative polarization state. We follow the reset pulse with a

programming/set pulse voltage for 1ms. The magnitude of these pulses varies from 0V to 4V with increments of 0.5V to all gates, i.e., we apply set pulses of all possible combinations on the three gates (total of $9 \times 9 \times 9 = 729$ individual combinations). The final drain current is measured by applying a 1ms pulse of $V_{DS} = 0.1V$ to obtain the output of the neuron. Fig. 2(c-k) shows how drain current, I_D changes with respect to one of the gate voltages (V_1) as the other two gate voltages (V_2/V_3) is varied from 0V to 4V, with an interval of 0.5V. We fit these experimental values with the outputs from our model, obtained under the same operating conditions. The final model parameters are listed in Supplementary Table S1. The corresponding floating gate voltages for the different drain currents are shown in Supplementary Fig. S5.

With the calibrated model, we can now compare the non-linear behavior of the device due to the partial polarization switching to a similar device with only capacitive coupling in its gates. To elucidate the importance of ferroelectric switching, we will look at how the device I_D changes with respect to one of the gate voltages (V_1) for different values of voltage set pulses applied to the other gates (V_2, V_3). Fig. 3(a–c) shows the I_D vs V_1 plots for three different sets of inputs. While the linear sum of the inputs V_2 and V_3 are all same for the three plots, the drain current varies significantly. In Fig. 3(a), we see that when V_2 and V_3 are small (1V), the device's threshold switching with respect to V_1 occurs at $\sim 1.5V$. However, for larger values, where more ferroelectric domains are able to switch in the other gates, the threshold with respect to V_1 is effectively lowered and we see non-zero drain current even at $V_1 = 0V$. Interestingly, we see that although the device turns on later with respect to V_1 , the drain current can actually be larger for the smaller V_2/V_3 case beyond $V_1 > 2V$. This can be explained by the fact that the larger gate voltage makes a greater contribution to the shared floating gate voltage, thus reducing the effective voltage across the ferroelectric layer of the first gate and thus results in fewer polarization switches and a lower drain current. Similar discussions hold true for the cases shown in Fig. 3(b) and (c) as well. Note, for our device all the gates are interchangeable as reflected by the different curves with same magnitudes but different order overlapping. In a purely capacitive setting, all the different voltages in the three different cases discussed above result in a simplistic summation of charges in the shared electrode (no non-linear polarization switching) and thus result in the same drain current characteristics. This can be simulated by turning off the polarization switching in our model by setting $P_S = 0$ and the results are shown in Fig. 3(d) – confirming our hypothesis.

In fact, the model allows us to vary various device and material parameters and observe the results to draw greater insights into the device behavior. For example, scaling of the ferroelectric capacitors laterally (i.e., reducing its area) reduces the number of domains that can be incorporated (27). Our simulations reveal that although this does make the device's behavior prone to more variability, the general switching characteristics remain quite similar, so long as the area ratio between the ferroelectric capacitors and FET remains the same (Supplementary Fig. S6). This is very encouraging from a scaling point of view and can be easily understood by looking at Eq.3. Reducing the ferroelectric layer thickness (i.e., vertical scaling), however, results in a greater change in behavior (Supplementary Fig. S7) under the same operating conditions. Again, referring to Eq. 3, we see that this is owed to a two-fold impact: (a) increase in the effective electric field across the ferroelectric layer, which induces more polarization switching, and (b) increase of capacitance; both being inversely proportional to thickness. To highlight the effect of only the polarization term, we can analyze different intrinsic activation fields. Supplementary Fig. S8 and S9 show the cases where the means of the gaussian activation field distribution are $1MV/cm$ and

5MV/cm respectively. Here, a higher nominal value of activation field results in fewer polarization switching events. This yields a smaller polarization term, which in turn makes the device behavior more capacitive in nature, especially when the applied voltage is small (see similarities to Fig. 3(d)). In contrast, a lower activation field allows for greater polarization switching even at smaller voltages. In our following discussion, we incorporate this device model into a co-simulation framework to investigate the co-design possibilities and potential of the device in network-level learning scenarios.

Network-level Performance Evaluation:

The multi-gate device structure lends itself to being integrated directly into crossbar implementations of neural networks similar to prior neuronal device implementations. Fig. 4(a,b) shows the proposed network and its corresponding architectural circuit implementation. Instead of all the weights of a column being connected to a single neuronal device, each gate is connected to a subset of weights, i.e., if there are d dendritic branches/input gates and n weights per column of the crossbar, each gate is connected to $k = n/d$ connections randomly selected without replacement. Thus, each synaptic weight is only connected to a single input gate. Note, this only needs to be done once during network initialization and therefore does not incur any overhead in hardware implementation. Now, as each gate is connected to only k weights, instead of n , this significantly reduces the required crossbar array size. In reality, crossbar size is dependent on various factors (32) and as they are scaled, non-idealities in the device-level (stochastic write operations, process variations) and circuit-level (driver/sensing resistance, sneak paths, interconnect parasitics, analog-to-digital/digital-to-analog converter nonlinearity) compound, leading to inefficiencies and erroneous operation. Thus, instead of a single large crossbar, it is generally broken into multiple crossbar arrays, whose outputs are later summed together. This summation operation is generally performed in the digital domain, thereby requiring costly analog-to-digital converters and storage of intermediate values – eschewing the efficiency gains of in-memory computation. In comparison, our device and algorithm framework allows us to avoid this by performing all computations in the analog domain, while preserving the benefits afforded by the use of smaller crossbar arrays.

The inputs are applied concurrently across the gates. Mathematically, the floating gate voltage can be written as:

$$\phi_F \propto g\left[\sum_{l=1}^d \mathbf{S}_l \odot \mathbf{W} \odot \mathbf{x}\right] \quad (8)$$

Here, \mathbf{x} is the incoming input to the crossbar, \mathbf{W} denotes the weight vector of the crossbar column, \mathbf{S}_l is a binary masking vector that indicates whether the weight is connected to the l -th branch and $g[\cdot]$ is the dendritic non-linearity offered by the ferroelectric. To extract this nonlinearity from our device model, we look at the floating gate voltage with respect to one of the gate voltages while setting the others to ground (Supplementary Fig. S10). Taking inspiration from the Preisach model of ferroelectric switching (33), we abstract the branch non-linear function as a hyperbolic tangent. Since only positive input voltages are considered, we set the function equal to zero for all negative values. Likewise, the final drain current is another non-linear function of the floating gate potential and acts as the final output of the entire neuron for that column. For this, a rectified linear unit (ReLU) is selected (Supplementary Fig. S4) for training our neural network. The impact of the device characteristics on network-level tasks is evaluated next.

We analyze the proposed network for learning tasks by combining our device model into a device-circuit-algorithm co-simulation framework. We train the networks on the Fashion-MNIST (34) dataset (Fig. 4(c)). The network consisted of $28 \times 28 = 784$ input neurons followed by 2 hidden layers with each layer having P neurons with k dendritic branches for each neuron and an output layer with 10 neurons. The neurons in the hidden layers utilize our developed device model. When k is equal to zero, it represents a network with neurons with no dendritic branches. Details regarding the simulation can be found in the Methods section.

We start off by comparing the results of a network with dendrites ($k = 3$) using the multi-gate FeFETs to a network which does not employ dendrites ($k = 0$) – ideal software ReLU neurons. Note, both the types of networks employ the same architecture with equivalent weight parameters and only differ in their neuronal operation. As illustrated in Fig. 4(d), we find that as the number of trainable weight patterns are varied, the resultant test accuracy of networks without dendrites achieve a maximum accuracy of 90.03% and decrease as the number of parameters is reduced. In contrast, the dendritic network is able to achieve better accuracies with networks with fewer number of parameters. In fact, we find that the maximum accuracy obtained by the networks without dendrites can be achieved by a dendritic network that uses $\sim 17 \times$ fewer parameters (> 1 order of magnitude improvement). Further improvements are possible for dendritic networks by sampling the weights to the different branches using a variety of strategies, rather than random selection (13). This result highlights that employing the multi-gate Ferroelectric FETs can significantly cut down on required resources (chip area, power, etc.) for computing – making them ideal for applications related to edge intelligence.

Next, we explored how network accuracy changes as the number of parameters and number of branches, k , are varied independently (Fig. 4(e)). We compare the difference of test accuracies with an equivalent network (same number of trainable parameters) with no dendrites ($k = 0$) and find that the performance scales and saturates as the number of branches is increased. It is also observed that the improvement owing to dendritic branches are greater as the number of parameters are decreased, further elucidating the impact of the dendritic network. It should be noted that device-level non-idealities (inter-gate parasitics, leakage, sneak paths, etc.) can become a factor as k is increased, which can lead to errors in operation. We have not considered such effects for our first-order analysis in this work.

To explain the apparent advantage owing to using dendritic networks, we explore how dendrites help to increase the network's complexity or expressivity. It has been shown that non-linear perceptrons divide the input space by hyperplanes (35). Generally, the more hyperplanes dividing the input space, the greater the network's complexity (36). To explore this empirically using visuals, we train a small network on scikit-learn's (37) concentric circles dataset, where data points are sampled from two circles of differing radius. It is a classic 2D non-linear problem, which cannot be effectively solved with a linear network. We train two versions of small networks with 2 input neurons, 2 hidden layer neurons and 2 output neurons, one with dendrites ($k = 2$) and the other without ($k = 0$). After training, we plot the decision boundary of the two networks along with the test dataset, as shown in Supplementary Fig. S11. We find that the network without dendrites is only able to separate the input space with 2 planes, whereas the network with dendrites is able to more accurately wrap around the inner circle to differentiate the two sets of points. Although this is a very simplistic simulation, it still elucidates the increased complexity afforded by the non-

linearity of dendrites that lies at the center of this improvement, i.e. such a functionality would not be possible without the ferroelectric layer.

Discussion

In summary, we propose a multi-gate FeFET as a neuron with dendritic branches. We incorporate an experimentally calibrated device model of the neuron into a device-circuit-algorithm co-simulation framework and clearly highlight the advantage afforded by such a hardware implementation in comparison to networks without dendrites. This work in combination with prior efforts on ferroelectric synapses (27, 28) can pave the path forward for a fully integrated learning framework for future resource constrained edge devices.

Methods

Device Fabrication: The multi-gate FeFET device is built on a p-type silicon substrate. The n-type source and drain regions are created with ion implantation. A 10nm HfO₂ layer deposited with atomic layer deposition (ALD) functions as the gate dielectric. The ferroelectric capacitors incorporate a metal-ferroelectric-metal (MFM) architecture with a W/Hf_{0.5}Zr_{0.5}O₂/W stack. First, 50nm thick Tungsten bottom electrode was deposited via sputtering. 10nm thick ferroelectric Hf_{0.5}Zr_{0.5}O₂ (HZO) thin films were deposited via ALD at 250°C, utilizing Hf[N(C₂H₅)CH₃]₄ and Zr[N(C₂H₅)CH₃]₄ as Hafnium and Zirconium precursors, respectively, with oxygen serving as the oxidant. Zirconium concentration was regulated through adjustment of the hafnium-to-zirconium precursor cycle ratio. Following lithographic patterning, 50nm thick Tungsten top electrodes were deposited via sputtering. Subsequently, bottom electrode vias were etched to facilitate electrical connections. The orthorhombic ferroelectric phase within the HZO layer was induced through Rapid Thermal Annealing (RTA) at approximately 500°C for 1 minute under Nitrogen atmosphere.

Electrical Characterization: The device characterization is performed with Keithley 4200-SCS Semiconductor Characterization System. All gate capacitors maintained uniform dimensions of 50µm×50µm. Multiple polarization states in the ferroelectric gates were achieved through the application of incremental voltage pulses, yielding a broad spectrum of current responses, as illustrated in Figure 2. For parallel programming operations, discrete write pulses were administered independently to individual capacitors connected in parallel. All the capacitors underwent initialization with a -3V reset pulse of 1ms duration. Subsequently, pulses with amplitudes ranging from 0V to 4V, in 0.5V increments and with consistent 1ms duration, were applied. Transfer characteristics were then obtained by varying the gate-source voltage across different polarization states.

Network Simulation: The network is constructed in Python using the PyTorch library (38). We train the network using the Adam optimizer (39) and employ the cross-entropy function to calculate the loss. Batch normalization (40) and dropout of 0.5 (41) were utilized for regularization. Both versions of the network (with and without dendrites) were trained over 100 epochs with a learning rate that is exponentially decaying from 10⁻² to 10⁻⁵. We used a batch-size of 64 for the training process.

References:

1. W. S. McCulloch, W. Pitts, A logical calculus of the ideas immanent in nervous activity. *Bull. Math. Biophys.* **5**, 115–133 (1943).
2. G. Stuart, N. Spruston, H. Michael, others, *Dendrites* (Oxford University Press, 2016).
3. P. Poirazi, B. W. Mel, Impact of active dendrites and structural plasticity on the memory capacity of neural tissue. *Neuron.* **29**, 779–796 (2001).
4. C. Koch, T. Poggio, V. Torre, Nonlinear interactions in a dendritic tree: localization, timing, and role in information processing. *Proc. Natl. Acad. Sci.* **80**, 2799–2802 (1983).
5. P. Poirazi, T. Brannon, B. W. Mel, Pyramidal neuron as two-layer neural network. *Neuron.* **37**, 989–999 (2003).
6. X. E. Wu, B. W. Mel, Capacity-enhancing synaptic learning rules in a medial temporal lobe online learning model. *Neuron.* **62**, 31–41 (2009).
7. A. Tzilivaki, G. Kastellakis, P. Poirazi, Challenging the point neuron dogma: FS basket cells as 2-stage nonlinear integrators. *Nat. Commun.* **10**, 3664 (2019).
8. S. Hussain, S.-C. Liu, A. Basu, "Improved margin multi-class classification using dendritic neurons with morphological learning" in *2014 IEEE International Symposium on Circuits and Systems (ISCAS)* (2014), pp. 2640–2643.
9. X. Wu, X. Liu, W. Li, Q. Wu, Improved expressivity through dendritic neural networks. *Adv. Neural Inf. Process. Syst.* **31** (2018).
10. I. S. Jones, K. P. Kording, Might a single neuron solve interesting machine learning problems through successive computations on its dendritic tree? *Neural Comput.* **33**, 1554–1571 (2021).
11. R.-L. Wang, Z. Lei, Z. Zhang, S. Gao, Dendritic convolutional neural network. *IEEJ Trans. Electr. Electron. Eng.* **17**, 302–304 (2022).
12. Z. Zhang, Z. Lei, M. Omura, H. Hasegawa, S. Gao, Dendritic learning-incorporated vision transformer for image recognition. *IEEE/CAA J. Autom. Sin.* **11**, 539–541 (2024).
13. S. Chavlis, P. Poirazi, Dendrites endow artificial neural networks with accurate, robust and parameter-efficient learning. *Nat. Commun.* **16**, 943 (2025).
14. C. Liu, J. Ma, S. Li, D. D. Zhou, Dendritic Integration Inspired Artificial Neural Networks Capture Data Correlation. *Adv. Neural Inf. Process. Syst.* **37**, 79325–79349 (2024).
15. X. Li, J. Tang, Q. Zhang, B. Gao, J. J. Yang, S. Song, W. Wu, W. Zhang, P. Yao, N. Deng, others, Power-efficient neural network with artificial dendrites. *Nat. Nanotechnol.* **15**, 776–782 (2020).
16. S. Liu, D. Akinwande, D. Kireev, J. A. C. Incorvia, Graphene-Based Artificial Dendrites for Bio-Inspired Learning in Spiking Neuromorphic Systems. *Nano Lett.* (2024).
17. S. D'agostino, F. Moro, T. Torchet, Y. Demiraug, L. Grenouillet, N. Castellani, G. Indiveri, E. Vianello, M. Payvand, DenRAM: neuromorphic dendritic architecture with RRAM for efficient temporal processing with delays. *Nat. Commun.* **15**, 3446 (2024).
18. K. Boahen, Dendrocentric learning for synthetic intelligence. *Nature.* **612**, 43–50 (2022).
19. H. J.-Y. Chen, M. Beauchamp, K. Toprasertpong, F. Huang, L. Le Coeur, T. Nemeč, H.-S. P. Wong, K. Boahen, "Multi-gate FeFET Discriminates Spatiotemporal Pulse Sequences for Dendrocentric Learning" in *2023 International Electron Devices Meeting (IEDM)* (2023), pp. 1–4.
20. J. Edwards, L. Parker, S. G. Cardwell, F. S. Chance, S. Koziol, "Neural-Inspired Dendritic Multiplication Using a Reconfigurable Analog Integrated Circuit" in *2024 IEEE International Symposium on Circuits and Systems (ISCAS)* (2024), pp. 1–5.
21. S. Ramakrishnan, R. Wunderlich, J. Hasler, S. George, Neuron array with plastic synapses and programmable dendrites. *IEEE Trans. Biomed. Circuits Syst.* **7**, 631–642 (2013).

22. S. Roy, A. Basu, An online unsupervised structural plasticity algorithm for spiking neural networks. *IEEE Trans. neural networks Learn. Syst.* **28**, 900–910 (2016).
23. G. Lee, H. J. Kim, E. J. Shin, S. Kim, T. I. Lee, B. J. Cho, A novel split-gate ferroelectric FET for a compact and energy efficient neuron. *IEEE Electron Device Lett.* **43**, 1375–1378 (2022).
24. S. Deng, M. Benkhelifa, S. Thomann, Z. Faris, Z. Zhao, T.-J. Huang, Y. Xu, V. Narayanan, K. Ni, H. Amrouch, "Compact ferroelectric programmable majority gate for compute-in-memory applications" in *2022 International Electron Devices Meeting (IEDM)* (2022), pp. 36–37.
25. H. Lee, D.-H. Choe, S. Jo, J.-H. Kim, H. H. Lee, H.-J. Shin, Y. Park, S. Kang, Y. Cho, S. Park, others, Unveiling the origin of robust ferroelectricity in sub-2 nm hafnium zirconium oxide films. *ACS Appl. Mater. & Interfaces.* **13**, 36499–36506 (2021).
26. K. A. Aabrar, S. G. Kirtania, F.-X. Liang, J. Gomez, M. San Jose, Y. Luo, H. Ye, S. Dutta, P. G. Ravikumar, P. V. Ravindran, others, BEOL-compatible superlattice FEFET analog synapse with improved linearity and symmetry of weight update. *IEEE Trans. Electron Devices.* **69**, 2094–2100 (2022).
27. A. N. M. N. Islam, A. Saha, Z. Jiang, K. Ni, A. Sengupta, Hybrid stochastic synapses enabled by scaled ferroelectric field-effect transistors. *Appl. Phys. Lett.* **122**, 123701 (2023).
28. A. Saha, A. N. M. N. Islam, Z. Zhao, S. Deng, K. Ni, A. Sengupta, Intrinsic synaptic plasticity of ferroelectric field effect transistors for online learning. *Appl. Phys. Lett.* **119**, 133701 (2021).
29. T. Shibata, T. Ohmi, A functional MOS transistor featuring gate-level weighted sum and threshold operations. *IEEE Trans. Electron Devices.* **39**, 1444–1455 (2002).
30. S. Deng, G. Yin, W. Chakraborty, S. Dutta, S. Datta, X. Li, K. Ni, "A Comprehensive Model for Ferroelectric FET Capturing the Key Behaviors: Scalability, Variation, Stochasticity, and Accumulation" in *2020 IEEE Symposium on VLSI Technology* (2020), pp. 1–2.
31. C. Alessandri, P. Pandey, A. Abusleme, A. Seabaugh, Monte Carlo simulation of switching dynamics in polycrystalline ferroelectric capacitors. *IEEE Trans. Electron Devices.* **66**, 3527–3534 (2019).
32. S. Jain, A. Sengupta, K. Roy, A. Raghunathan, {Rx-Caffe}: Framework for evaluating and training Deep Neural Networks on Resistive Crossbars. *arXiv Prepr. arXiv1809.00072* (2018).
33. K. Ni, M. Jerry, J. A. Smith, S. Datta, "A circuit compatible accurate compact model for ferroelectric-FETs" in *2018 IEEE symposium on VLSI technology* (2018), pp. 131–132.
34. H. Xiao, K. Rasul, R. Vollgraf, Fashion-mnist: a novel image dataset for benchmarking machine learning algorithms. *arXiv Prepr. arXiv1708.07747* (2017).
35. G. F. Montufar, R. Pascanu, K. Cho, Y. Bengio, On the number of linear regions of deep neural networks. *Adv. Neural Inf. Process. Syst.* **27** (2014).
36. M. Raghu, B. Poole, J. Kleinberg, S. Ganguli, J. Sohl-Dickstein, "On the expressive power of deep neural networks" in *international conference on machine learning* (2017), pp. 2847–2854.
37. F. Pedregosa, G. Varoquaux, A. Gramfort, V. Michel, B. Thirion, O. Grisel, M. Blondel, P. Prettenhofer, R. Weiss, V. Dubourg, others, Scikit-learn: Machine learning in Python. *J. Mach. Learn. Res.* **12**, 2825–2830 (2011).
38. A. Paszke, S. Gross, F. Massa, A. Lerer, J. Bradbury, G. Chanan, T. Killeen, Z. Lin, N. Gimelshein, L. Antiga, others, Pytorch: An imperative style, high-performance deep learning library. *Adv. Neural Inf. Process. Syst.* **32** (2019).
39. D. P. Kingma, J. Ba, Adam: A Method for Stochastic Optimization (2017), (available at <https://arxiv.org/abs/1412.6980>).
40. S. Ioffe, Batch normalization: Accelerating deep network training by reducing internal

covariate shift. *arXiv Prepr. arXiv1502.03167* (2015).

41. N. Srivastava, G. Hinton, A. Krizhevsky, I. Sutskever, R. Salakhutdinov, Dropout: a simple way to prevent neural networks from overfitting. *J. Mach. Learn. Res.* **15**, 1929–1958 (2014).

Acknowledgments

The authors would like to acknowledge GlobalFoundries Dresden Germany for providing FeFET testing devices.

Funding: This material is based upon work supported in part by the U.S. National Science Foundation under award No. #2318101 and #2346953. The electrical characterization is supported by the U.S. Department of Energy, Office of Science, Office of Basic Energy Sciences Energy Frontier Research Centers program under Award Number DESC0021118.

Author contributions: A.N.M.N.I. and A.S. proposed and conceptualized the project. X.N., J.D., S.K. performed the device fabrication and characterization. The device modeling and network simulation was performed by A.N.M.N.I. All authors contributed to the writing of the manuscript. K.N and A.S. supervised the project.

Competing interests: Authors declare that they have no competing interests.

Data and materials availability: All data needed to evaluate the conclusions in the paper are present in the paper and/or the Supplementary Materials.

Figures

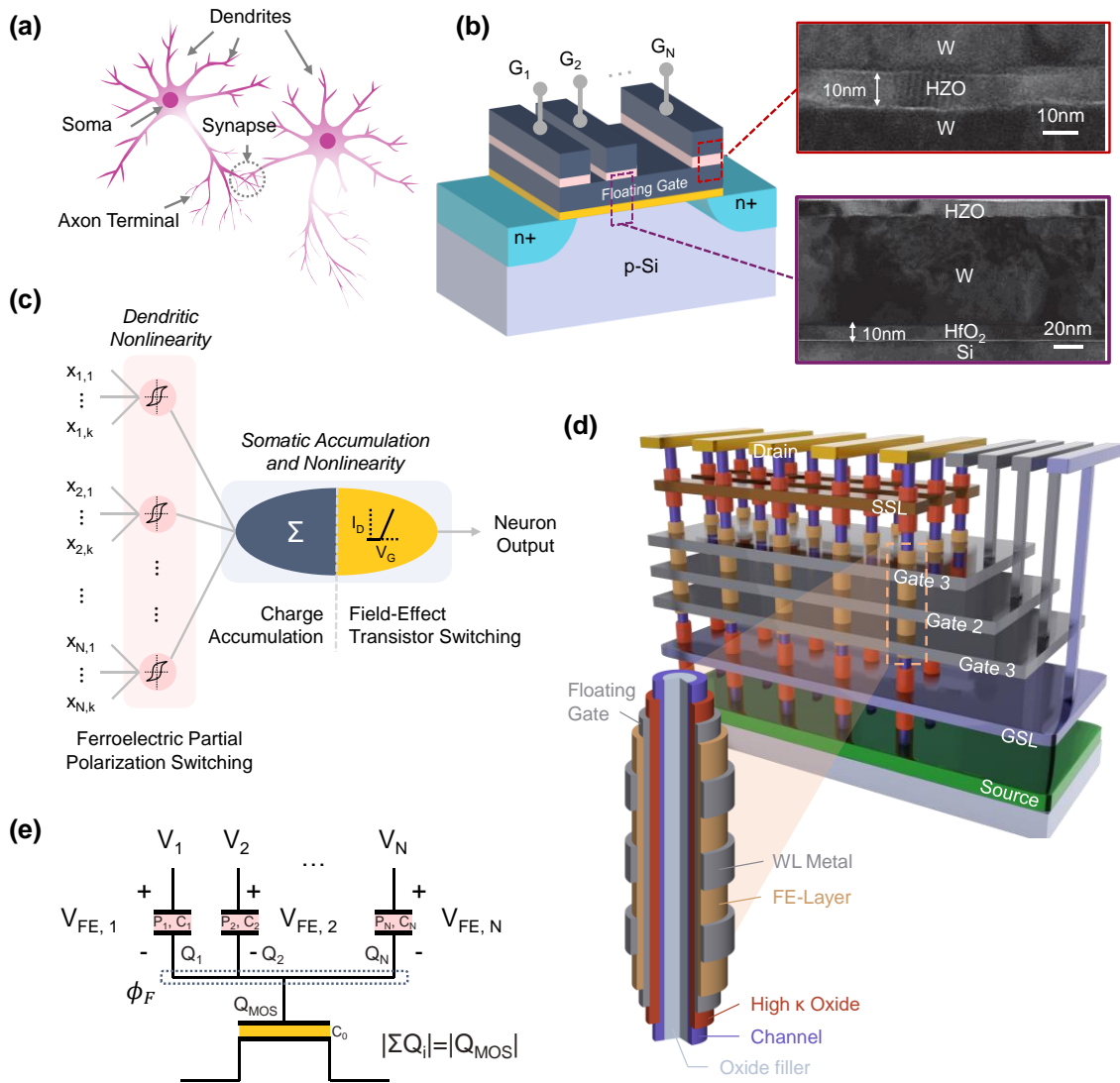


Fig. 1. Overview of Dendritic Computing with Multi-gate FeFET. (a) Signal from one neuron's axon terminals travel to the next neuron's dendrites through the synaptic cleft. It reaches the neuron's cell body or soma and is then propagated forward. (b) An n -gate FeFET structure along with the Transmission Electron Microscopy (TEM) cross-sectional images of the material stack. (c) The dendritic nonlinearity is mapped to the partial polarization switching of the ferroelectric layer, while the somatic accumulation occurs through charge accretion at the shared floating gate. The somatic nonlinearity is mapped to the FET switching characteristics. (d) The scalability and back-end-of-line compatibility of the ferroelectric layers enables us to integrate the multi-gate FeFET device vertically in 3D architectures to ensure high density. The devices are interfaced with ground select transistors/line (GSL) and string select transistors/line (SSL) for proper operation. (e) The multi-gate device symbol. Its structure can be abstracted as multiple ferroelectric capacitors connected in parallel with a FET in series connection below. The partial polarization switching characteristics induces a non-linear component to the floating gate voltage (ϕ_F), which then modifies the channel characteristics to obtain the modulated drain current, the final neuronal output.

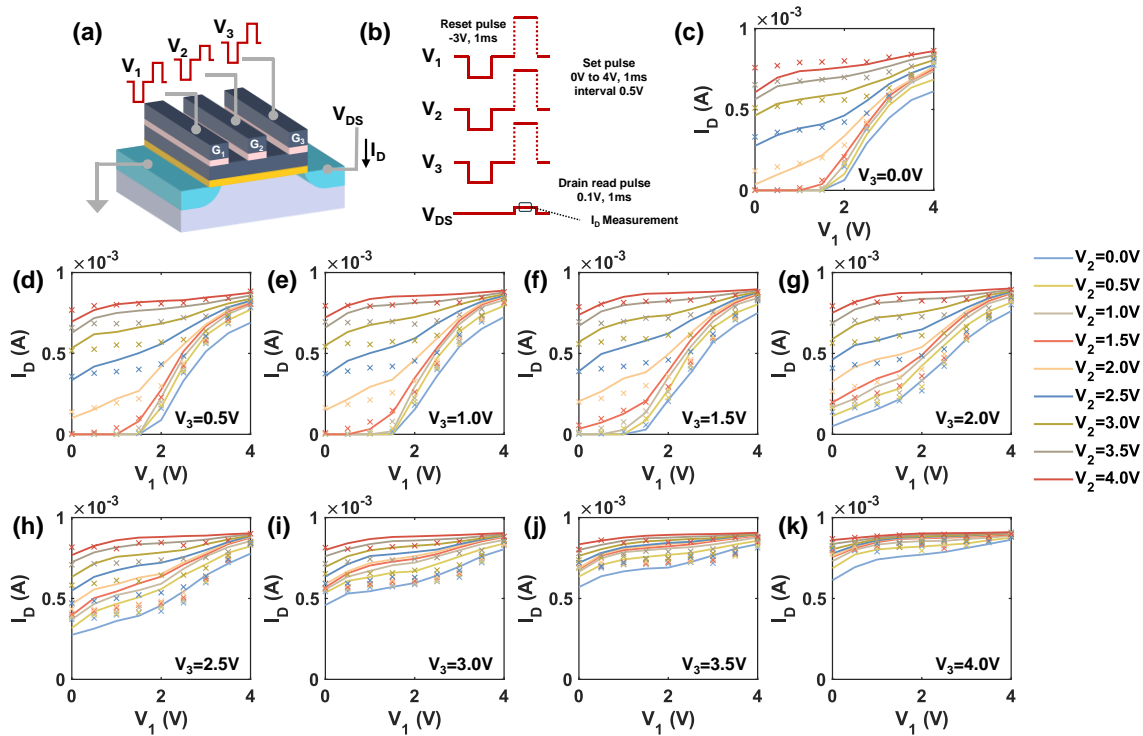


Fig. 2. Characterization of Neuronal Behavior of the Multi-gate FeFET. (a) Experimental setup for measuring the multi-gate FeFET characteristics (3-gates). (b) Each gate receives a reset pulse followed by a set/programming pulse, during which the drain current is measured for an applied drain voltage, V_{DS} . (c-k) Drain current I_D with respect to applied set voltage to the first gate, V_1 . For each panel, the different colored curves represent different set pulse values applied to the second gate, V_2 . Likewise, the set voltage applied to the third terminal, V_3 remains constant for each panel and is noted at the bottom right of the panel. It should be noted that the gates are interchangeable, and the same results can be obtained by selecting any other relative combination. The calibrated model (solid lines) matches well with the experimental data (represented with \times 's).

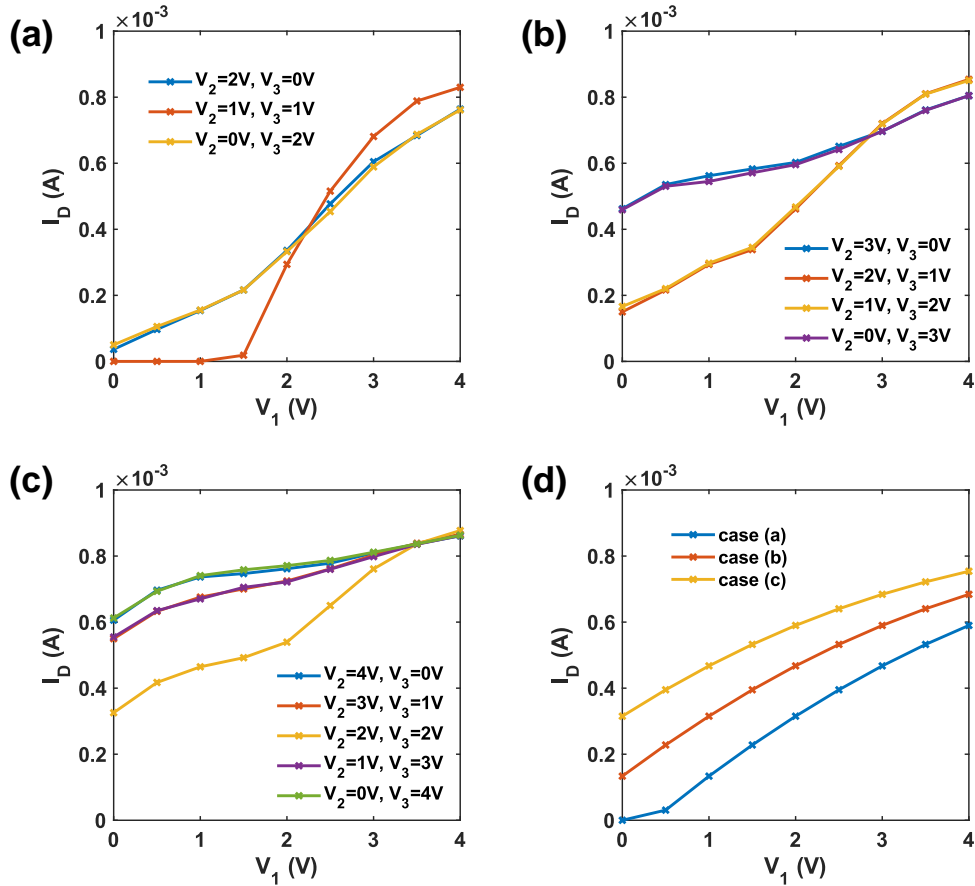


Fig. 3. Impact of Ferroelectric Non-linear Switching. Drain current, I_D as one of the gate voltages (V_1) is swept from 0V to 4V for different amplitudes of V_2 and V_3 for our multi-gate dendritic device. **(a)** $V_2 = 2V, V_3 = 0V$; $V_2 = 1V, V_3 = 1V$ and $V_2 = 0V, V_3 = 2V$, **(b)** $V_2 = 3V, V_3 = 0V$; $V_2 = 2V, V_3 = 1V$; $V_2 = 1V, V_3 = 2V$ and $V_2 = 0V, V_3 = 3V$, **(c)** $V_2 = 4V, V_3 = 0V$; $V_2 = 3V, V_3 = 1V$; $V_2 = 2V, V_3 = 2V$; $V_2 = 1V, V_3 = 3V$ and $V_2 = 0V, V_3 = 4V$. Due to the nonlinear interactions, the I_D curves vary for the different cases. Note, all the gates are interchangeable. **(d)** Drain current, I_D vs. gate voltage V_1 with purely capacitive dendritic gates for the input voltage cases shown in (a) – (c). The inputs overlap as there is no non-linear component in the accumulation.

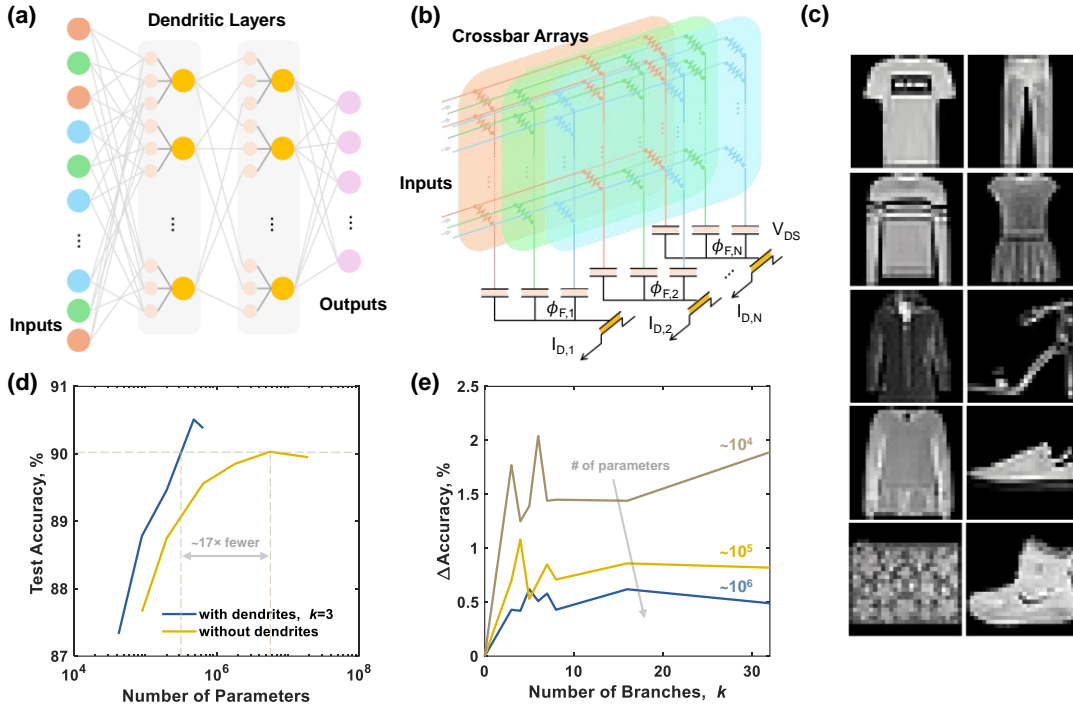


Fig. 4. Network-level Performance evaluation. (a) The proposed deep dendritic neural network architecture with $k = 3$ dendritic branches. In each dendritic layer, each branch is connected to a subset of the previous layer. We have color-coded the input layer to show how they are connected to different branches. These dendritic layers can be stacked to create deep architectures. (b) The circuit architecture of the proposed dendritic layer. Each color, like (a), denotes a separate crossbar array that is interfaced with different gates of our device. For applied drain voltage, V_{DS} , the resultant drain currents are the outputs for the next layer. This architecture allows us to optimize our device based on the crossbar array size. (c) The Fashion-MNIST dataset, consisting of grayscale images assorted into 10 categories, was used for training and evaluating the network-level performance of networks with and without dendrites. (d) Test accuracy of networks with and without dendrites. Dendritic functionality is enabled by the multi-gate FeFET. We find that the network with dendrites is able to achieve equivalent performance to much larger (in terms of trainable weight parameters) networks without dendrites. (e) Performance improvements ($\Delta Accuracy$) on the test set, with respect to a network with equal trainable weight parameters but no dendrites. It is revealed that the efficacy of the dendrites increases as the total number of parameters decreases.

Supplementary Materials for
Dendritic Computing with Multi-gate Ferroelectric Field-Effect Transistors

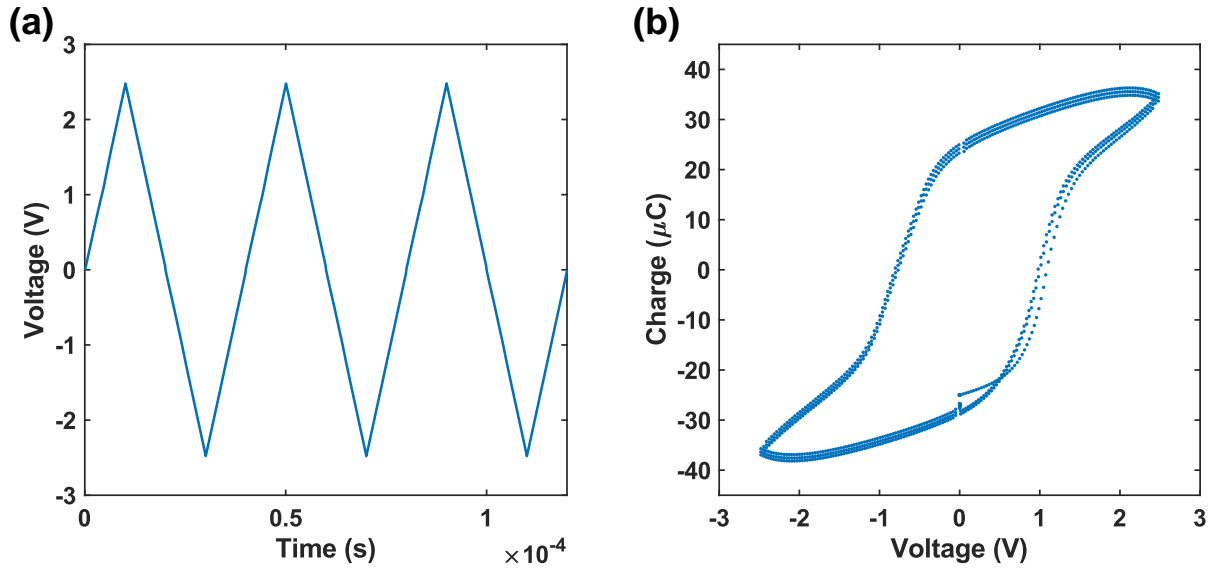
A N M Nafiul Islam *et al.*

*Corresponding author: Abhronil Sengupta. Email: sengupta@psu.edu

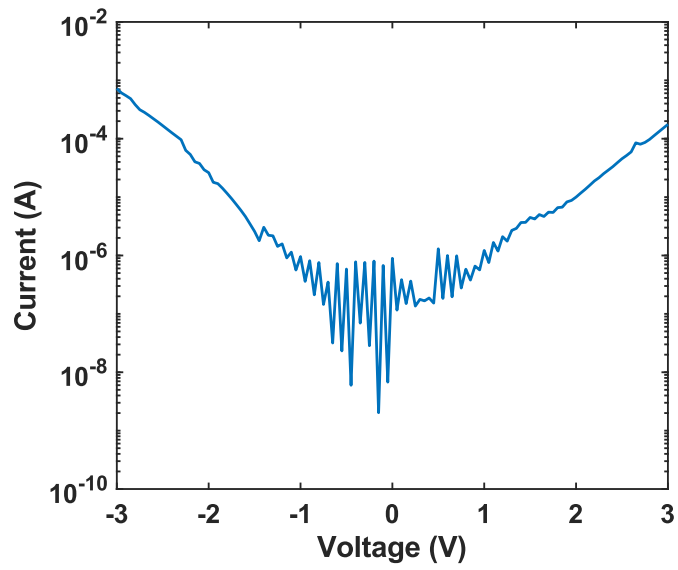
This PDF file includes:

Supplementary Figs. S1 to S11
Supplementary Table S1

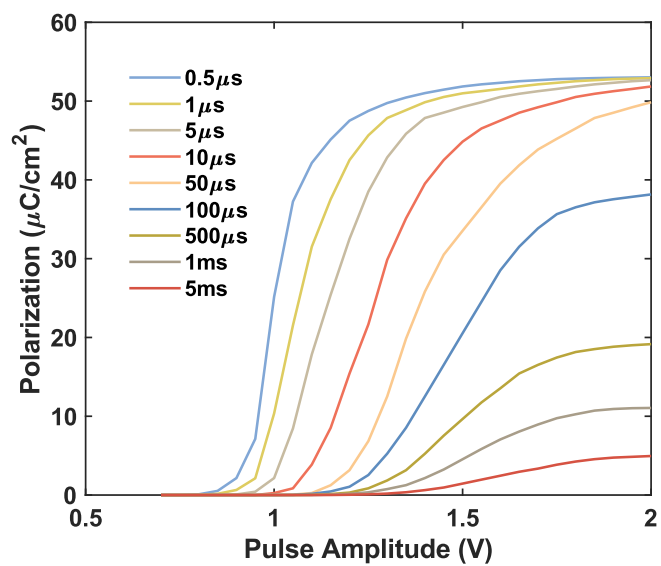
Supplementary Figures



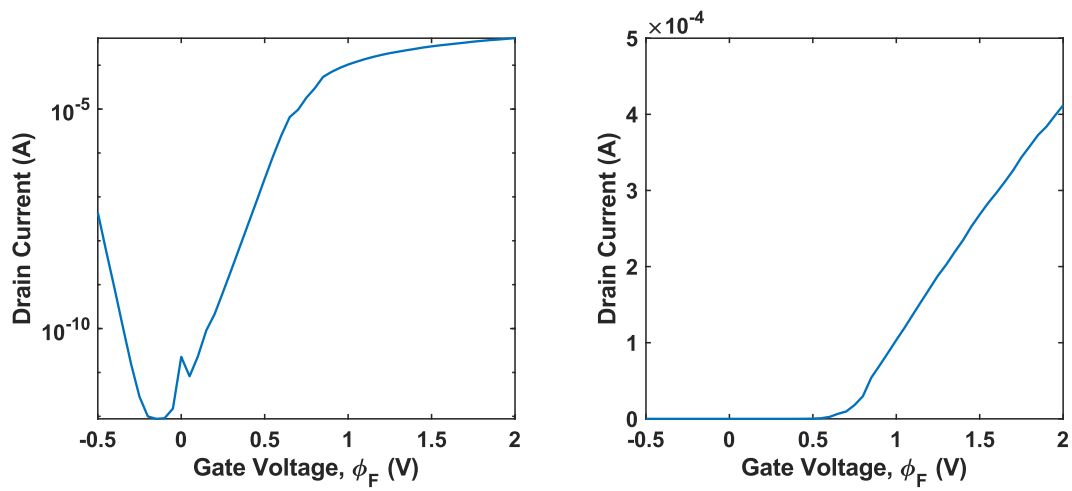
Supplementary Fig. S1: Polarization switching observed for the ferroelectric capacitors in the gate stack. **(a)** Input voltage to the capacitor is a triangular wave with an amplitude of 2.5V and time period of $40\mu\text{s}$. **(b)** Charge vs voltage characteristics of the ferroelectric capacitor. The hysteresis indicates the ferroelectric polarization switching.



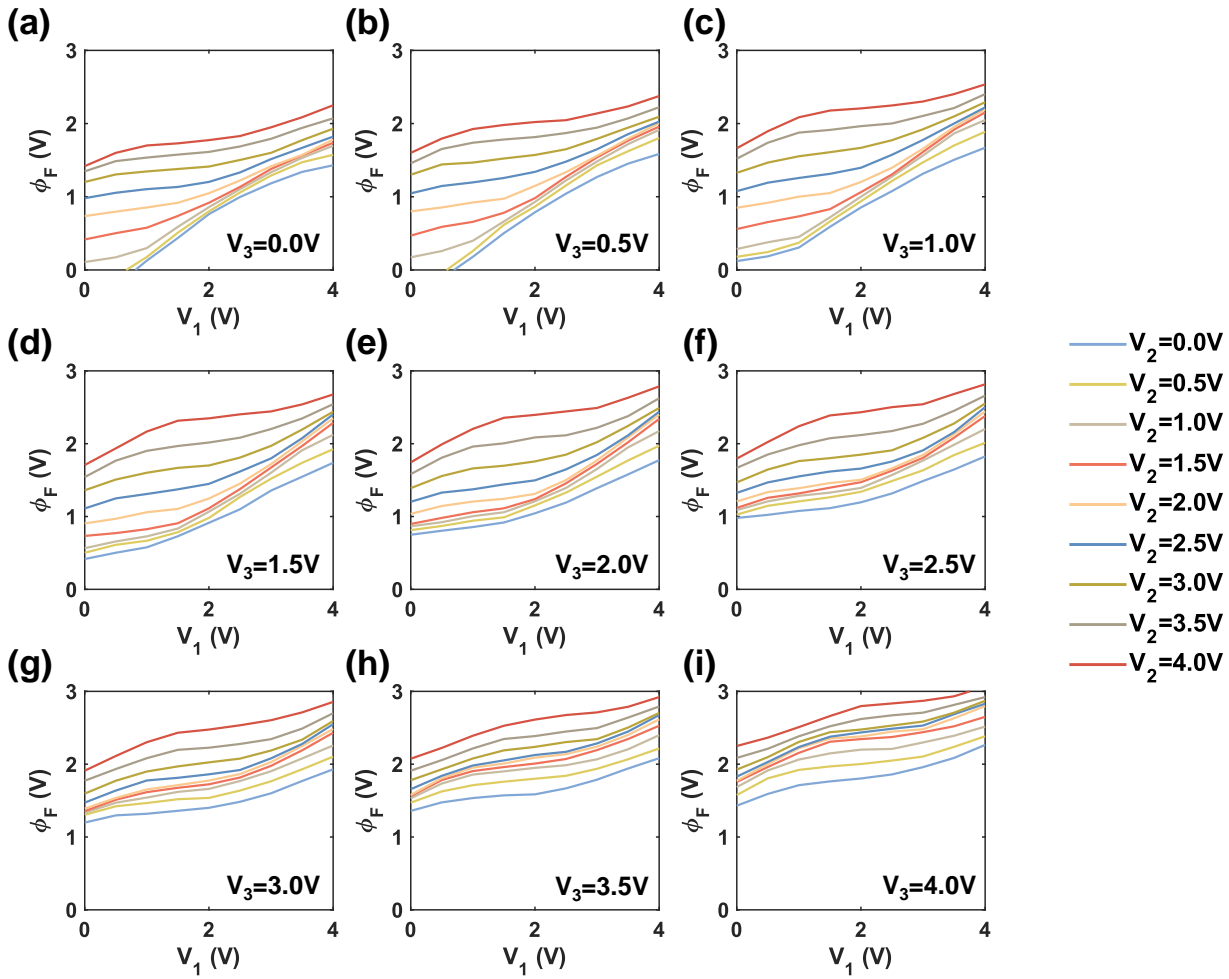
Supplementary Fig. S2: Experimental DC current-voltage characteristics of the ferroelectric capacitors in the gate stack.



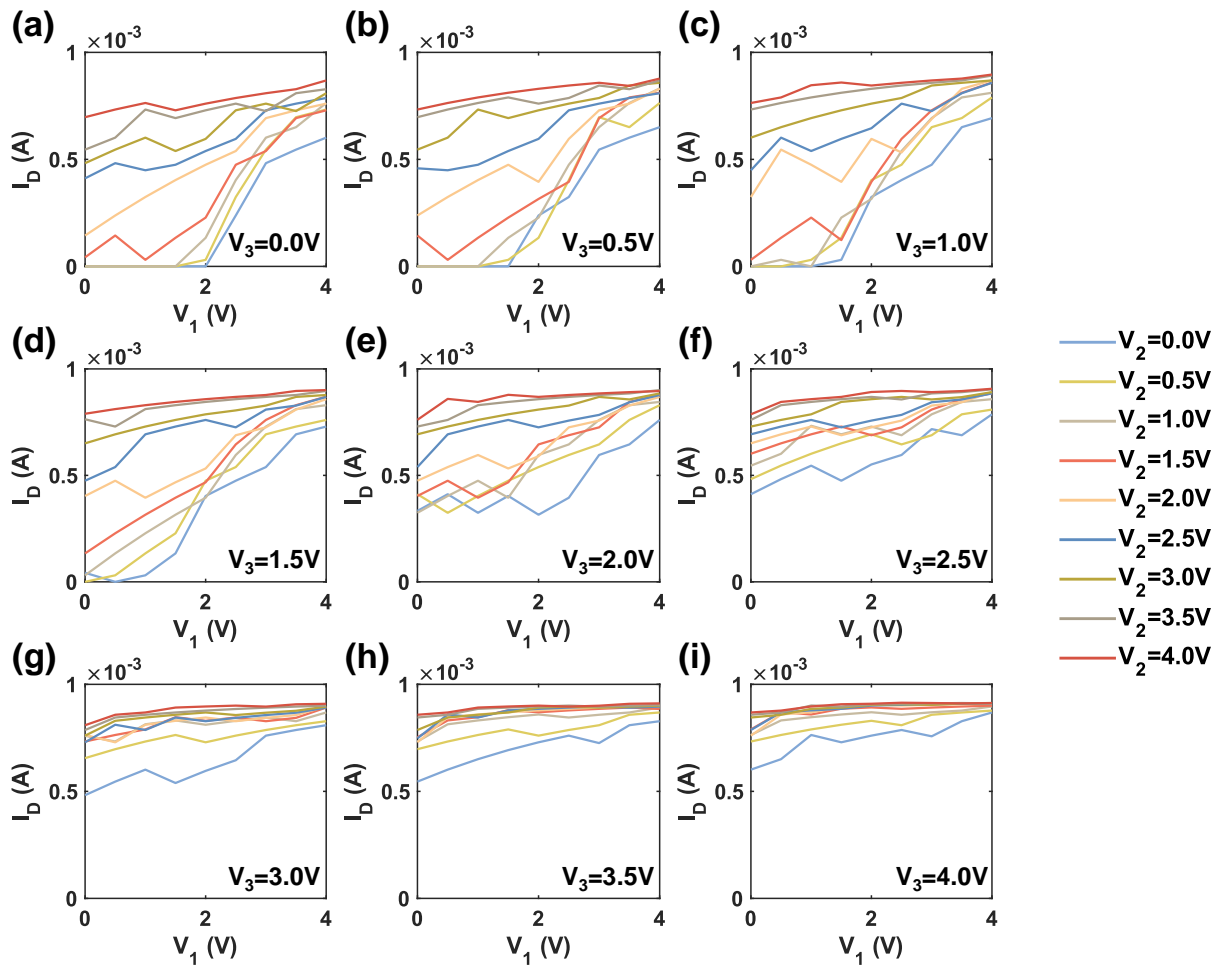
Supplementary Fig. S3: Change of Polarization with respect to voltage pulses of different amplitudes and widths.



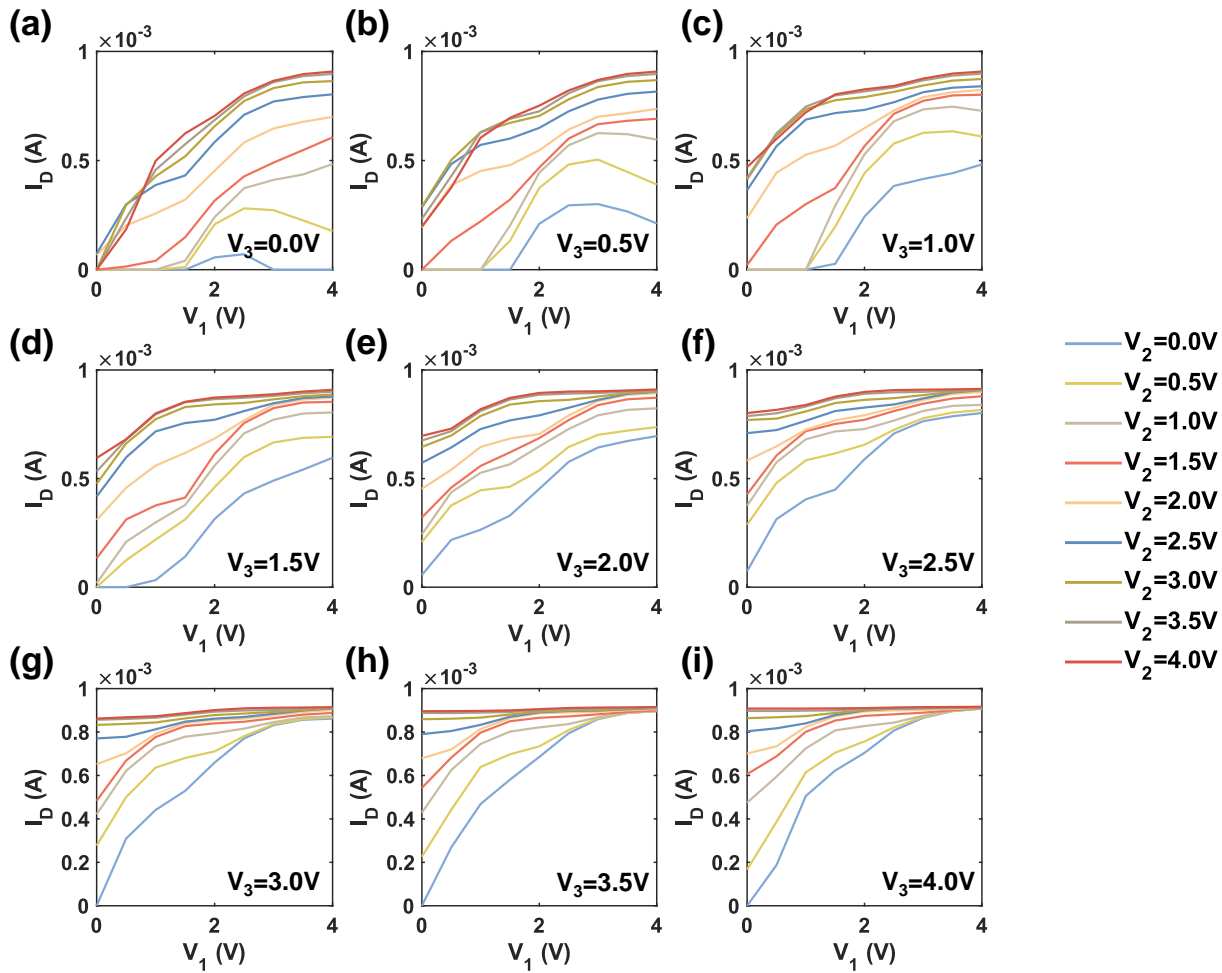
Supplementary Fig. S4: Field Effect Transistor transfer characteristics obtained by sweeping the gate voltage ϕ_F from $-0.5V$ to $2V$ and measuring the drain current with an applied drain voltage of $0.1V$ in logarithmic scale (**left**) and linear scale (**right**).



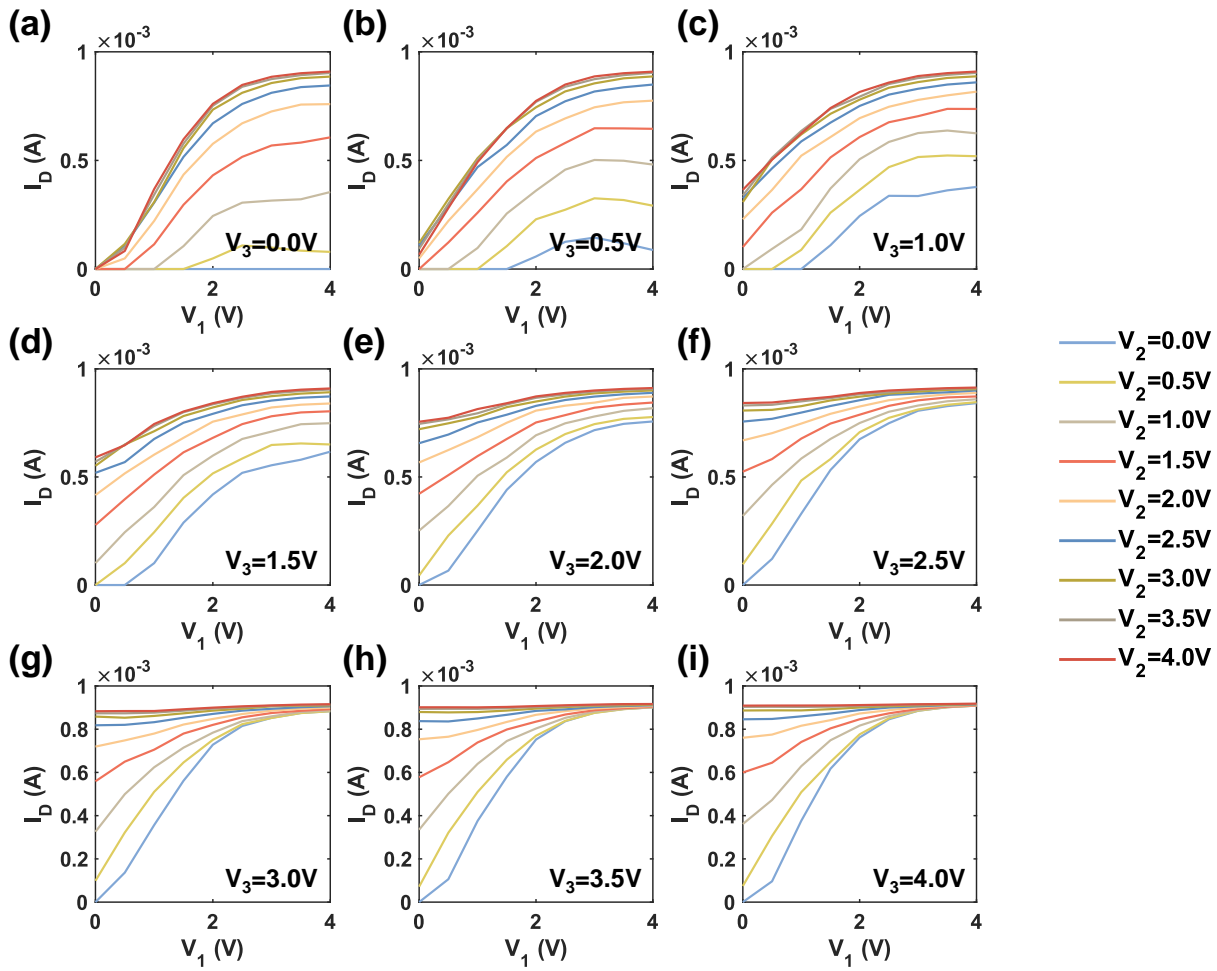
Supplementary Fig. S5: Floating gate voltage, ϕ_F with respect to applied set voltage to the first gate, V_1 for the multi-gate FeFET corresponding to same conditions as Fig. 2(c-k) of the main text. (a-i) For each panel, the different colored curves represent different set pulse values applied to the second gate, V_2 . Likewise, the set voltage applied to the third terminal, V_3 remains constant for each panel and is noted at the bottom right of the panel.



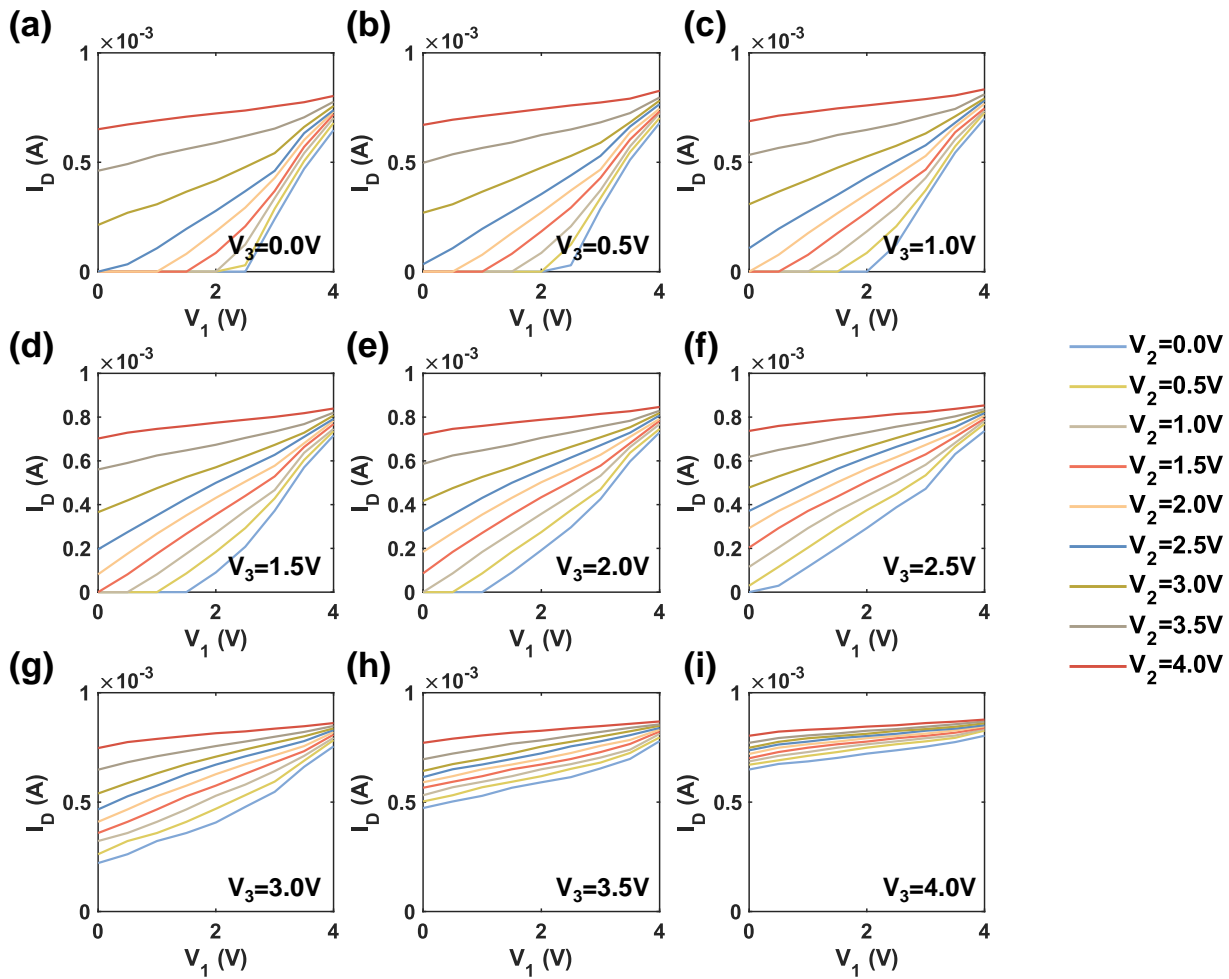
Supplementary Fig. S6: Drain current I_D with respect to applied set voltage to the first gate, V_1 for a multi-gate FeFET with scaled ferroelectric capacitors. For the simulation, we chose the number of domains, N_{dom} to be 20, according to findings in (29). **(a-i)** For each panel, the different colored curves represent different set pulse values applied to the second gate, V_2 . Likewise, the set voltage applied to the third terminal, V_3 remains constant for each panel and is noted at the bottom right of the panel. We find that although the device behavior becomes somewhat erratic, the trend in the characteristics is preserved even when we consider scaling.



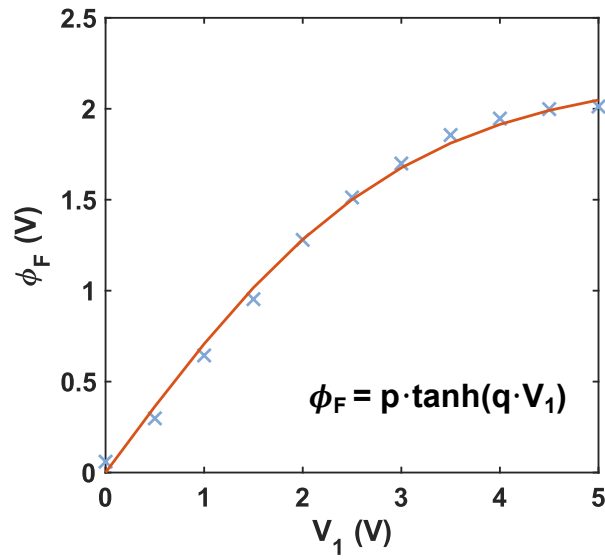
Supplementary Fig. S7: Drain current I_D with respect to applied set voltage to the first gate, V_1 for a multi-gate FeFET with scaled ferroelectric capacitors. For the simulation, we chose the ferroelectric layer thickness, t_{fe} to be $5nm$. **(a-i)** For each panel, the different colored curves represent different set pulse values applied to the second gate, V_2 . Likewise, the set voltage applied to the third terminal, V_3 remains constant for each panel and is noted at the bottom right of the panel.



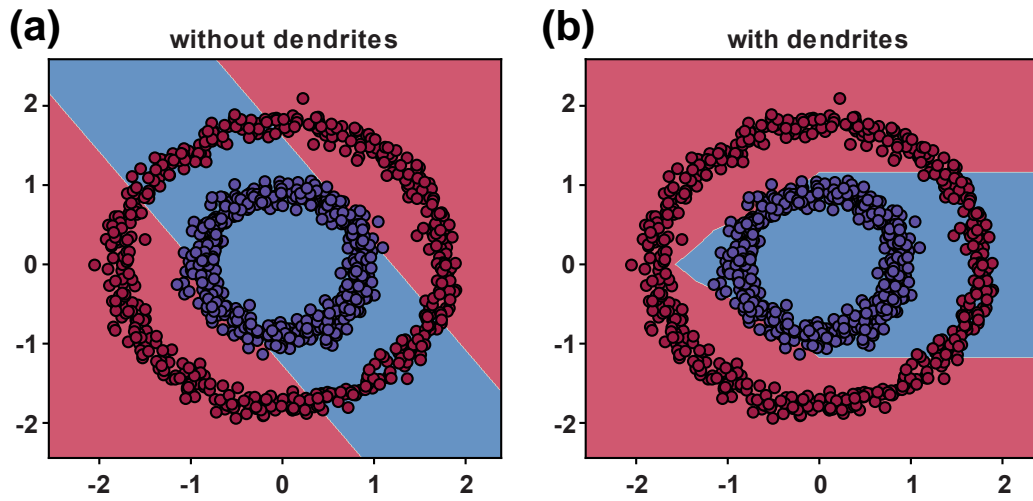
Supplementary Fig. S8: Drain current I_D with respect to applied set voltage to the first gate, V_1 for a multi-gate FeFET with scaled ferroelectric capacitors. For the simulation, we chose the mean of the activation field to be $1MV/cm$. (a-i) For each panel, the different colored curves represent different set pulse values applied to the second gate, V_2 . Likewise, the set voltage applied to the third terminal, V_3 remains constant for each panel and is noted at the bottom right of the panel.



Supplementary Fig. S9: Drain current I_D with respect to applied set voltage to the first gate, V_1 for a multi-gate FeFET with scaled ferroelectric capacitors. For the simulation, we chose the mean of the activation field to be $5MV/cm$. **(a-i)** For each panel, the different colored curves represent different set pulse values applied to the second gate, V_2 . Likewise, the set voltage applied to the third terminal, V_3 remains constant for each panel and is noted at the bottom right of the panel.



Supplementary Fig. S10: With the calibrated model, we extract the floating gate voltage, ϕ_F with respect to one of the gate voltages, V_1 , when $V_2/V_3 = 0$. Taking inspiration from the Preisach model of ferroelectric switching (31), we fit the data to the equation of form, $\phi_F = p \cdot \tanh(q \cdot V_1)$, where $p = 2.2$ and $q = 1/3$. We use this abstraction as the branch non-linearity to train our network.



Supplementary Fig. S11: Decision boundary for the concentric circles dataset with two classes for (a) a network without dendrites, $k = 0$ and (b) a network with dendrites, $k = 2$.

Supplementary Table S1. Device Model Parameters

Parameters	Value
Number of domains, N_{dom}	1000
Time-step, Δt	10 μs
Saturated polarization, P_s	28 $\mu C/cm^2$
Polarization time constant, τ_0	20ns
Time constant exponent, α	4.0
Activation field distribution, E_a	$\mathcal{N}(\mu = 3 MV/cm, \sigma = 1)$
Shape parameter, β	2
Temperature	300K
Substrate Doping	1 \times 10 ¹⁵ cm ⁻³
FET oxide thickness	10nm
Ferroelectric layer thickness	10nm
Read drain voltage	0.1V
Read source voltage	0V